

Accepted Manuscript

Myo-Inositol based nano-PCM for Solar Thermal Energy Storage

D.K. Singh, S. Suresh, H. Singh, B.A.J. Rose, S. Tassou, N. Anantharaman

PII: S1359-4311(16)31561-7

DOI: <http://dx.doi.org/10.1016/j.applthermaleng.2016.08.202>

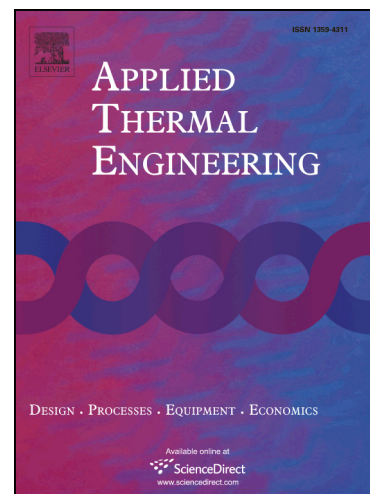
Reference: ATE 9001

To appear in: *Applied Thermal Engineering*

Received Date: 18 March 2016

Revised Date: 25 August 2016

Accepted Date: 28 August 2016



Please cite this article as: D.K. Singh, S. Suresh, H. Singh, B.A.J. Rose, S. Tassou, N. Anantharaman, Myo-Inositol based nano-PCM for Solar Thermal Energy Storage, *Applied Thermal Engineering* (2016), doi: <http://dx.doi.org/10.1016/j.applthermaleng.2016.08.202>

This is a PDF file of an unedited manuscript that has been accepted for publication. As a service to our customers we are providing this early version of the manuscript. The manuscript will undergo copyediting, typesetting, and review of the resulting proof before it is published in its final form. Please note that during the production process errors may be discovered which could affect the content, and all legal disclaimers that apply to the journal pertain.

Myo-Inositol based nano-PCM for Solar Thermal Energy Storage

D.K. Singh¹, S. Suresh^{1*}, H. Singh², B.A.J. Rose², S. Tassou², N. Anantharaman³

¹Department of Mechanical Engineering, National Institute of Technology, Tiruchirappalli, 620015, India

²Institute of Energy Futures, College of Engineering, Design and Physical Sciences, Brunel University London, Kingston Lane Uxbridge, UK

³Department of Chemical Engineering, National Institute of Technology, Tiruchirappalli, 620015, India

* (corresponding author) Email: ssuresh@nitt.edu

Keywords: Phase change material (PCM), Nanoparticles, Thermal cycling, Heat of fusion, Melting temperature, Solar thermal energy storage

Nomenclature

a, b, and c	crystal Unit cell parameters
α	The angle between b and c
β	The angle between a and c
γ	The angle between a and b
wt.	Weight
λ	Wavelength

Nm Nanometer

mW milliWatt

Abbreviation

PCM Phase change material

TES Thermal energy storage

MI Myo-inositol

DSC Differential scanning calorimetry

FT-IR Fourier transform-infra-red

XRD X-ray diffraction

SEM Scanning electron microscopy

FWHM Full width half maximum

JCPDS Joint committee on powder diffraction standards

MI-A Myo-inositol- alumina (Al_2O_3) nanoparticles

MI-C Myo-inositol-CuO nanoparticles

NPs Nanoparticles

FESEM Field emission scanning electron microscope

Greek symbol

θ Theta

Abstract

The thermo-physical behavior of Myo-Inositol (MI), (a sugar alcohol), was investigated as a potential material for developing more compact solar thermal energy storage systems than those currently available. This latent heat storage medium could be utilized for commercial and industrial applications using solar thermal energy storage in the temperature range of 160°C to 260°C, if its thermal performance was modified. The objective of this investigation was to determine via experimentation, if Al₂O₃ and CuO nanoparticles dispersed in pure MI for mixtures of 1, 2 and 3% (by weight) improved the thermal performance of MI for solar thermal energy systems. Nanoparticles only physically interacted with MI, and not chemically, even after 50 thermal cycles. The distribution of CuO nanoparticles in the nano-PCM was found to be more uniform than alumina nanoparticles. After cycling, nano-MIs studied here suffered a lower decrease in heat of fusion than pure MI, which makes nano-MIs more suitable for solar thermal storage applications at 160°C to 260°C. Between CuO and Al₂O₃ nanoparticles, latter was found to be more suitable for compact solar thermal energy storage owing to an increase in melting point observed.

1. Introduction

For meeting the increasing demand of energy, it is critical that energy is stored in the most efficient manner. PCMs such as sugar alcohols can potentially bridge the gap between peak heat demand and supply by storing energy in the form of latent heat due to their availability and suitable melting and

freezing temperature ranges. These have a narrow phase transition range that allows them to discharge thermal energy at nearly isothermal conditions. Many studies reporting the suitability of galactitol and D-mannitol as thermal storage media can be found in literature, though only a few have reported the behavior of Myo-inositol (MI). Aran et al. [1] experimentally studied cycling and chemical stability of sugar alcohols such as myo-inositol (MI), galactitol and D-mannitol. Myo-inositol underwent polymorphic changes when it was analyzed from 50°C to 260°C with no effect on the stability of MI. Heat of fusion decreased by approximately 30% when D-mannitol was cycled 20 times and by 50% when 50 cycles are performed. Galacitol showed poor cycling stability. Antoni et al. [2, 3] reported polymorphism in the case of D-mannitol though it did not affect the thermal behavior (melting temperature, enthalpy of fusion) from 135°C to 175°C. G. Kumarsen et al. [4] reported a thermal decomposition of D-mannitol, occurring at 300.15°C. Seul-Ye-Lee et al. [5] investigated the use of expanded graphite in erythritol and found that the thermal conductivity increased to 3.56 W/mK for the composite. However, this study was limited to only five thermal cycles.

Recently, the suspension of nanoparticles in the conventional PCMs (paraffin, etc.) is being increasingly researched into aimed at improving their thermo-physical properties. Kalaiselvam et al. [6] reported a reduction of 12.97% and 4.97% in the solidification time for the 60% n-tetradecane, 40% n-hexadecane PCM respectively with aluminum and alumina nanoparticles. Luo Zhicho et al. [7] reported an enhancement in the heat capacity of nano-titania laden erythritol by 40% in solid phase and 14% in liquid phase when a volume fraction of 0.2 volume % of nano-titania was used. Fugai et al. [8] reported not all metal particles are compatible with all PCMs, for example, aluminum is compatible with paraffin, while copper and nickel are not. Ho et al. [9] dispersed Al₂O₃ nanoparticles to paraffin with mass fraction of 5 and 10 wt. % and found decrease of 7 and 13 % in heat of fusion. While

thermal conductivity enhancement found to be 2 and 6 % respectively for 5 and 10 wt. % Al_2O_3 nanoparticles. Nourani et al. [10] investigated Al_2O_3 nanoparticles dispersed paraffin using sodium stearoyl lactylate as a surfactant and found that melting temperature of have composites 2.5, 5.0, 7.5 and 10.0 wt. % nano Al_2O_3 have 1.20, 1.50, 1.35 and 1.65 °C higher than those pure paraffin and decrease of 4.13 kJ/kg, 5.41 kJ/kg, 14.86 kJ/kg and 22 kJ/kg in heat of fusion observed.

Sharma et al. [11] studied palmitic acid- TiO_2 as nano-enhanced organic phase change material and found that melting temperature varied in the range of -0.26 and +2°C and latent heat of fusion between 2 % to 15.5 % and latent heat of fusion of palmitic acid was decreased by 17.88% after 1500 melt/freeze cycle. Fang et al. [12] studied eicosane/graphene nanoplatelets (GNPs) and found that average latent heat of fusion of the 1, 2, 5 and 10 wt. % composite is lower than that of pure eicosane by 0.5,1.7,5.4 and 16.0 % respectively and melting points of composites was shown nearly independent of loading of GNPs.

Till date no study has been reported on the characterization of nanoparticle impregnated MI. Hence, the aim of this study is to evaluate and characterize the latent heat storage potential of MI with and without nano-additives for compact solar latent heat storage applications in the temperature range of 160°C to 260°C. Thermal cycling tests have been performed on pure MI, pure MI with CuO and alumina (Al_2O_3) nanoparticles (particle size 40-50 nm) with mass fractions of 1, 2 and 3 wt. %. The measurements were performed over 50 charging-discharging cycles using differential scanning calorimetry (DSC), thermogravimetric analysis equipment (TGA), Fourier transform infra-red (FT-IR) spectroscopy, X-ray diffraction and Scanning Electron Microscope (SEM) to observe thermos-physical properties, mass change, molecular bonds and functional groups, the crystal size changes and the distribution of nanoparticles in MI.

2. Methodology

Commercially available 99% pure MI, chemical formula $C_6H_{12}O_6$, was obtained from (Spectrochem Pvt. Ltd, Mumbai, India) with a mass density of 1.75 gm/cm^3 , molecular weight of 180.16, melting range between 222°C and 227°C was employed. Alumina (Al_2O_3) and Copper oxide (CuO) nanoparticles (particle size 40-50 nm) were procured from Alfa Aesar, USA.

For thermal cycling process, an experimental set up consisting of constant temperature hot plate heater (fig. 1), was used. During charging 30 gm of the PCM (pure MI or MI mixed with nanoparticles, nano-MI) was heated using a hot plate from 30°C to 260°C in a glass beaker. The molten PCM was cooled normally from 260°C to room condition (30°C) by passive cooling. Calibrated J-type thermocouples (calibrated with constant temperature oil bath with temperature accuracy of $\pm 1^\circ\text{C}$) in conjunction with KEYSIGHT 34972A LXI data acquisition system were used to measure and record the temperature of PCM. The physical state of PCM during melting and solidification was confirmed visually. The temperature were recorded at 30 seconds intervals during melting and solidification.

3. Nano-MI

Al_2O_3 and CuO nanoparticles were uniformly mixed at 1, 2 and 3 wt. % to MI by using a low energy ball mill which was rotated for 2 hours at 200 rpm for uniform mixing using three stainless steel balls providing centrifugal force. Melting temperature, time taken for melting and the variation of melting point over 50 charging-discharging cycles were recorded, no major change observed for melting points during thermal cycling. The time taken for melting and freezing was about 10 mins, for each nano-MI suspension studied. Fig. 2 shows pure MI before and after 50 thermal cycles. Its color was found to

change gradually from initial white to dark brown-black at the end of 50th cycle. Similar color change behavior was observed for nano-MI suspensions after 50 cycles.

Sample of pure MI, MI-Al₂O₃ (MI-A) and MI-CuO (MI-C) weighing 10 mg were taken before beginning of the thermal cycling and at the end of 50th cycle for DSC and FT-IR tests. PerkinElmer DSC equipment (DSC 6000) was used for these tests. The test were carried out in N₂ atmosphere in the temperature range of 160°C to 260°C with a heating rate of 6°C/min. PerkinElmer TGA equipment (TGA 4000) was used for TGA tests. Material decomposition was characterized by the mass loss measured with a high-precision balance. A PerkinElmer FT-IR spectrometer (FT-IR spectrum two) with wavelength range from 8300-350 cm⁻¹ was employed for analyzing the chemical compatibility between pure MI and nanoparticles over wave number range of 4000 to 500 cm⁻¹ in steps of 4 cm⁻¹. X-ray diffraction analysis was performed on Rigaku Ultima III XRD equipment and nanoparticle distribution in the suspension was analyzed with a field emission scanning electron microscope (Carl Zeiss AG - Supra 25).

4. Result and discussion

The surface morphology of pure MI using field emission scanning electron microscope shown in fig. 3(a), indicates that MI particles are highly irregular in shapes and sizes. There were large difference in shapes and size among MI (highly irregular), alumina NPs (nearly spherical), and CuO NPs (nearly spherical). Fig. 3(b) shows alumina nanoparticles distribution throughout MI with certain aggregation, but still CuO NPs (nearly spherical) were more uniformly distributed in MI than alumina NPs as seen in fig 3(c). Alumina NPs were showed more sticking with large particles of MI as shown in fig 3 (b).

The X-ray diffraction patterns of pure MI-A and MI-C are shown in Fig. 4. The average crystallite size (D) has been calculated from the peak using Debye–Scherer’s relation, $D = 0.9\lambda/W \cos\theta$ where λ is the wavelength of X-ray and W is the full width of half maximum. From fig. 4 (a) by using X ray diffraction analysis (XRDA 3.1) and PCPDFWIN database (program version 2.01) , it is confirmed that MI has unit cell parameters of $a = 6.622$ (3), $b = 12.897$ (4), $c = 17.949$ (8), $\alpha = 90.00$, $\beta = 93.98$, $\gamma = 90.00$. In pure MI two strong diffraction peaks were observed at 28.88° and 31.10° whilst other peaks occurred at 14.72° , 17.46° , 18.76° and 20.25° . Crystal size and lattice strain were calculated to be 35.76 nm (accuracy $\pm 3\%$), 0.0062 respectively for pure MI. After adding nanoparticles prominent intensity changes are observed as presented in fig. 4 (b) and fig. 4 (c).

Table 1. shows the heat of fusion for pure MI, before thermal cycling, was measured to be 351.6 kJ/kg and for MI-A it was measured to be 355.2 kJ/kg, 320.3 kJ/kg, 324.1 kJ/kg respectively for 1, 2 and 3 wt. %. This amounts to a decrease of 8.9% and 7.8% respectively for 2 and 3 wt. % of MI-A when compared with pure MI. Interestingly, there was an insignificant rise of 1.0% in the heat of fusion in the case of 1 wt. % MI-A. The heat of fusion of pure MI after 50 cycles was measured to be 210.1 kJ/kg which was 40.24% less as compared to pure MI. After 50 charging-discharging cycles, heat of fusion for MI-A with 1, 2 and 3 wt. % was measured to be 276.3 kJ/kg, 263.8 kJ/kg, 253.5 kJ/kg respectively which have 22.2% , 17.6% and 21.2% lesser heat of fusion when compared to MI-A before thermal cycling began.

Table 2. shows MI-C with 1, 2 and 3 wt. % was found to have heat of fusion of 299.9 kJ/kg, 275.3 kJ/kg, 252.4 kJ/kg respectively before thermal cycling, which shows a decrease of 14.7% , 21.6% and 28.2% respectively when compared with uncycled pure MI. MI-C with 1, 2 and 3 wt. % exhibited a

decrease of 12.3%, 13.3% and 14.7 % respectively in heat of fusion after 50 thermal cycles on comparison with MI-C before thermal cycling.

Melting point of pure MI was measured to be 225.47°C, and for MI-A with 1, 2 and 3 wt. % it was found to increase by 0.96°C, 0.65°C and 0.88°C respectively, when compared to pure MI. After thermal cycling by 50 times, the melting point of pure MI was found to decrease by 2.57°C and similarly for MI-A with 1, 2 and 3 wt. %, the melting point decreased by 3.25°C, 2.52°C and 3.65°C respectively when compared with corresponding MI-A solutions before thermal cycling.

In the case of MI-C with 1, 2 and 3 wt. % CuO, it was observed that there was a decrease of 1.37°C, 2.07°C, and 2.87°C in melting points when compared with pure MI before cycling. After 50 cycles there was a decrease of 0.5°C, 0.64°C, and 1.1°C in melting point as compared to MI-C with 1, 2 and 3 wt. % before cycling. Furthermore, reduction in melting points of MI-C was lesser when compared to counterpart MI-A solutions after 50 thermal cycles.

From the view point of thermal storage media, MI-A is more desirable as compared to MI-C due to a lower reduction in the heat of fusion on addition of nanoparticles.

FTIR equipment was used to measure the transmission spectra of Pure MI, MI-A and MI-C, see fig. 7 and fig. 8. Functional groups present in the pure MI are detailed in table 3. There was an indication of reaction with nitrogen, and some halogens during thermal cycling. Same functional groups were observed on addition of Al₂O₃ and CuO NPs to pure MI. MI-A samples exhibited a larger decrease in transmission compared to MI-C samples though. Major functional groups are strong O-H (usually stretching vibration) and CH₃, CH₂ and CH (2 or 3 bands) with wavenumbers 3218.66 cm⁻¹ and 2921.09 cm⁻¹ in pure MI which has infra-red transmission of 88.1% and 79.37 % respectively. After

adding alumina NPs with 1.0, 2.0 and 3.0 wt. % showed transmission 71.1%, 14.1% and 50.5% respectively for 3218.66 cm^{-1} wavenumber and 41.8%, 41.8% and 71.1% respectively for 2921.09 cm^{-1} wavenumber. In MI-C with 1.0, 2.0 and 3.0 wt. % it showed transmission of 79.2%, 72.1% and 88.6% respectively for 3218.66 cm^{-1} wavenumber and 88.5%, 84.6% and 86.1% for 2921.09 cm^{-1} wavenumber.

After the 50th cycle a slight decrease in transmission in the functional group region (4000 to 1500 cm^{-1}) for all MI-A and MI-C samples can be seen in fig. 7, though this fluctuation was less compared to those without cycling, as shown in fig. 7, fig. 8 and in table 1. It indicates that pure MI and nano-MI with alumina and CuO nanoparticles were chemically stable even after 50 cycles of melting and solidification. It can be inferred that MI and nanoparticles only interacted thermo-physically and no chemical interaction took place.

TGA curves detailing any change in mass of pure MI, MI-A and MI-C due to thermal cycling are shown in Fig. 9. Pure MI was observed to be highly stable with a less than 1 % mass change after 50 thermal cycles. MI-A and MI-C showed a mass change of less than 2 % before thermal cycling when tested using TGA equipment at 160°C - 260°C . After 50 cycles MI-A and MI-C mass changed by <3 %. Maximum mass change was observed for pure MI-A with 1.48 % at 2.0 wt. % and the minimum mass change was showed by pure MI-C with 0.65 % at 1.0 wt. % after 50 cycles. Such a low change in mass establishes the excellent suitability of MI and nano-MIs, MI-A and MI-C, for solar thermal energy storage in temperature range of 160°C to 260°C .

To date the exact mechanism for increase or decrease in heat of fusion of PCMs on addition of nanoparticles has not been agreed upon [13]. This phenomenon may depend upon factors such as

concentration of nanoparticles in the nano-PCM, size of NPs, their physical properties and the interaction between nanoparticles and PCM. A possible explanation of increase of heat of fusion for MI-A with 1 wt. % Al_2O_3 nanoparticles is the formation of local heat sinks in the form of aggregates by alumina nanoparticles. Decrease in the heat of fusion for MI-A with 2 and 3 wt. % alumina and MI-C with 1, 2 and 3 wt. % can be caused by a decreased amount of heat transmitted to the main functional group of MI (Strong stretching vibration O-H group, CH_3 , CH_2 , CH (2 or 3 bands) groups and strong CH_2 group).

5. Conclusion

Thermal, physical and chemical characteristics of pure MI and its nano-suspensions with alumina and CuO nanoparticles with 1, 2 and 3 wt. % have been experimentally studied using DSC and FT-IR. DSC results showed slight increase and decrease in melting points respectively for MI-A and MI-C. After 50 cycles, MI-A showed 2°C to 4°C decrease in melting point and MI-C 0.5°C - 1.1°C . Addition of nanoparticles reduced the magnitude of reduction in the heat of fusion compared to pure MI due to the processing over 50 charging-discharging cycles. Pure MI and alumina nanoparticles laden MI were observed to have an excellent chemical stability over a temperature range of 160°C to 260°C . The mass changes observed were less than 3% after thermal cycling for nano-MIs in the temperature range of 160°C to 260°C . After cycling, nano-MIs studied here suffered a lower decrease in heat of fusion than pure MI. This makes nano-MIs more suitable for solar thermal storage. A very low decrease in melting points and mass even after 50 thermal cycles makes the nano-MIs reliable for long term use. Based on the results, myo-inositol based nano-PCMs could be recommended as a potential material for solar thermal energy storage applications at 160°C to 260°C . Between CuO and Al_2O_3 nanoparticles,

latter was found to be more suitable for compact solar thermal energy storage owing to an increase in melting point observed.

Acknowledgement

Authors would like to acknowledge the funding obtained for the UKIERI-DST Thematic partnership (IND/CONT/E/14-15/381 and DST/INT/UK/P-105/2014) and in-kind support of industrial partner, M/s. Bharat Heavy Electrical Ltd., which made this research possible.

6. Reference.

- [1] Solé A, Neumann H, Niedermaier S, Martorell I, Schossig P, Cabeza LF. Stability of sugar alcohols as PCM for thermal energy storage. *Solar Energy Materials and Solar Cells*. 2014 Jul 31; 126:125-34.
- [2] Barreneche C, Gil A, Sheth F, Fernández AI, Cabeza LF. Effect of d-mannitol polymorphism in its thermal energy storage capacity when it is used as PCM. *Solar Energy*. 2013 Aug 31; 94:344-51.
- [3] Gil A, Barreneche C, Moreno P, Solé C, Fernández AI, Cabeza LF. Thermal behaviour of d-mannitol when used as PCM: comparison of results obtained by DSC and in a thermal energy storage unit at pilot plant scale. *Applied Energy*. 2013 Nov 30; 111:1107-13.
- [4] Kumaresan G, Velraj R, Iniyar S. Thermal analysis of d-mannitol for use as phase change material for latent heat storage. *Journal of Applied Sciences*. 2011 Dec; 11:3044-8.
- [5] Lee SY, Shin HK, Park M, Rhee KY, Park SJ. Thermal characterization of erythritol/expanded graphite composites for high thermal storage capacity. *Carbon*. 2014 Mar 31; 68:67-72.

- [6] Kalaiselvam S, Parameshwaran R, Harikrishnan S. Analytical and experimental investigations of nanoparticles embedded phase change materials for cooling application in modern buildings. *Renewable Energy*. 2012 Mar 31; 39(1):375-87.
- [7] Zhichao L, Qiang Z, Gaohui W. Preparation and enhanced heat capacity of nano-titania doped erythritol as phase change material. *International Journal of Heat and Mass Transfer*. 2015 Jan 31; 80:653-9.
- [8] Fukai J, Kanou M, Kodama Y, Miyatake O. Thermal conductivity enhancement of energy storage media using carbon fibers. *Energy Conversion and Management*. 2000 Sep 30; 41(14):1543-56.
- [9] Ho CJ, Gao JY. Preparation and thermophysical properties of nanoparticle-in-paraffin emulsion as phase change material. *International Communications in Heat and Mass Transfer*. 2009 May 31; 36(5):467-70.
- [10] Nourani M, Hamdami N, Keramat J, Moheb A, Shahedi M. Thermal behavior of paraffin-nano- Al_2O_3 stabilized by sodium stearyl lactylate as a stable phase change material with high thermal conductivity. *Renewable Energy*. 2016 Apr 30; 88:474-82.
- [11] Sharma RK, Ganesan P, Tyagi VV, Metselaar HS, Sandaran SC. Thermal properties and heat storage analysis of palmitic acid- TiO_2 composite as nano-enhanced organic phase change material (NEOPCM). *Applied Thermal Engineering*. 2016 Apr 25; 99:1254-62.
- [12] Fang X, Fan LW, Ding Q, Wang X, Yao XL, Hou JF, Yu ZT, Cheng GH, Hu YC, Cen KF. Increased thermal conductivity of eicosane-based composite phase change materials in the presence of graphene nanoplatelets. *Energy & Fuels*. 2013 Jun 13; 27(7):4041-7.

[13] Chieruzzi M, Miliozzi A, Crescenzi T, Torre L, Kenny JM. A new phase change material based on potassium nitrate with silica and alumina nanoparticles for thermal energy storage. *Nanoscale research letters*. 2015 Jun 28; 10 (1):1.

ACCEPTED MANUSCRIPT

Highlights

- Properties of Myo-Inositol laden with Al_2O_3 and CuO nanoparticles was studied.
- The melting point was found to increase for MI-A and decrease for MI-C.
- MI interacted only physically on addition of NPs.
- Mass changes were $<3\%$ after thermal cycling of MI-A and MI-C.
- MI-A is more suited for thermal energy storage than MI-C.

ACCEPTED MANUSCRIPT

Table 1. Phase change properties of pure MI and MI-A before and after thermal cycling

MI-A wt. %	Phase change peak temperature (°C)		Latent heat (kJ/kg)	
	Melting	Melting (50 cycles)	Melting	Melting (50 cycles)
0.0	225.5	222.9	351.6	210.1
1.0	226.4	223.9	355.2	276.3
2.0	226.2	223.6	320.3	263.8
3.0	226.4	222.7	324.1	253.5

Table 2. Phase change properties MI-C before and after thermal cycling

MI-C wt. %	Phase change peak temperature (°C)		Latent heat (kJ/kg)	
	Melting	Melting (50 cycles)	Melting	Melting (50 cycles)
1.0	224.1	223.6	299.9	262.4
2.0	223.4	222.8	275.3	238.7
3.0	222.6	221.5	252.4	215.1

Table 3. Functional groups present in pure MI, MI-A and MI-C before and after thermal cycling

Wavenumber (cm ⁻¹)	Functional group
3218.66	Strong, O-H, usually stretching vibration
2921.09	CH ₃ , CH ₂ and CH (2 or 3 bands)
1415.93	Strong CH ₂
1370.48	Medium O-H bonding in plane
1322.00	C-N amine stretching
928.74	C-H bonding vibration strong
1013.45	C-F (strong)
581.52	C-Br (strong)
1322.12	C-N (strong)

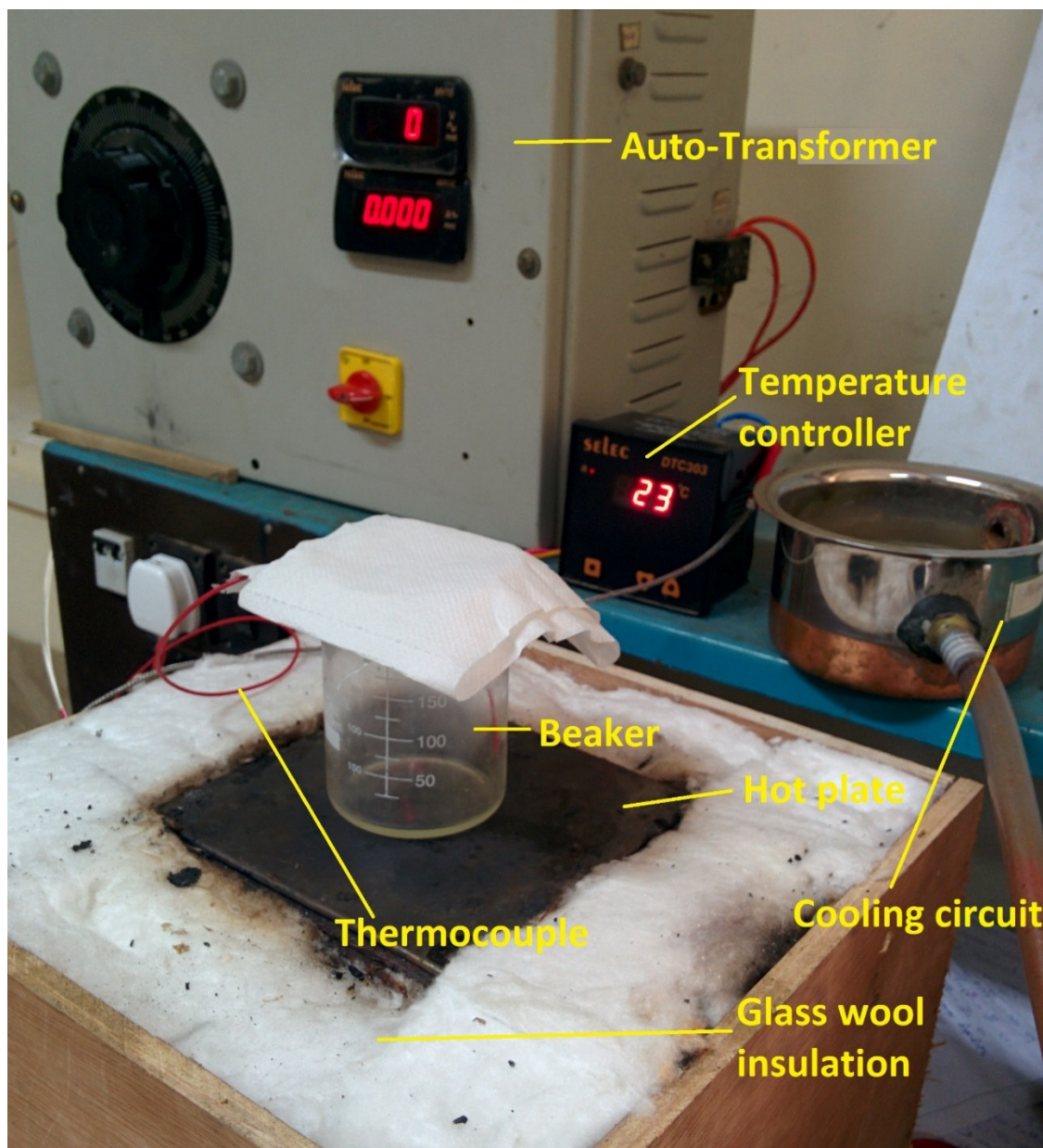
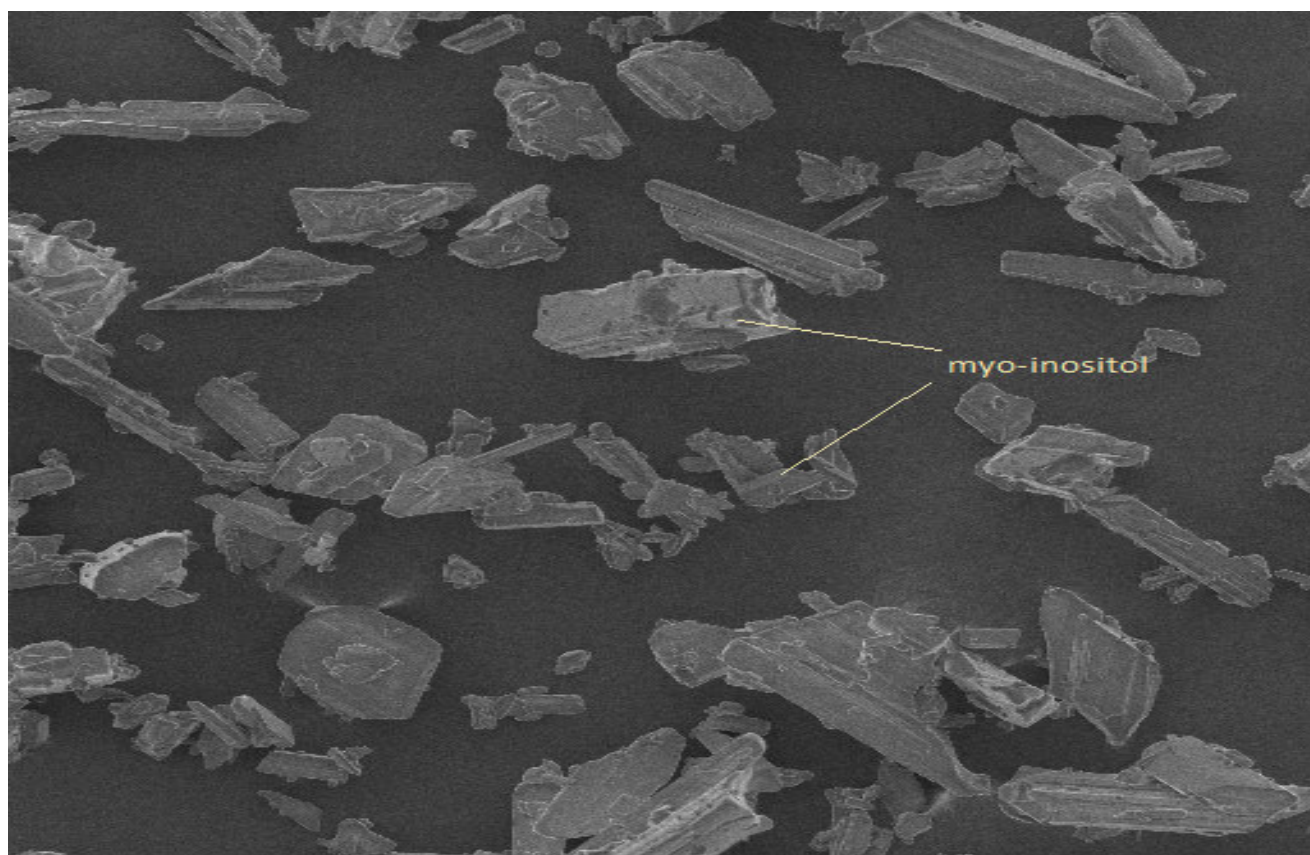


Fig. 1. Experimental set-up consisting of the hot plate, temperature sensing and control system



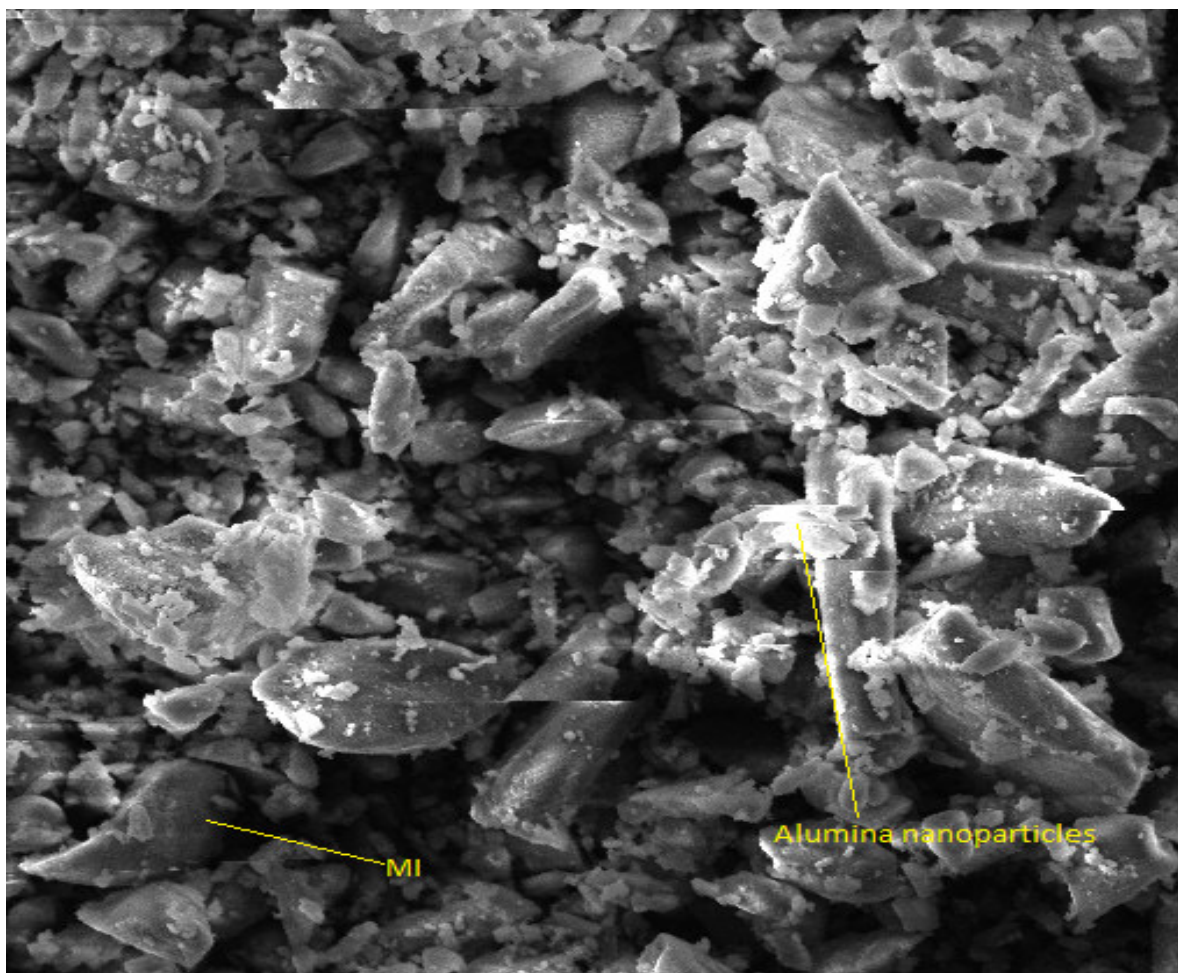
Fig. 2. Colour transition of pure MI from white before thermal cycling (left) to dark brown after 50th thermal cycle (right)

ACCEPTED MANUSCRIPT



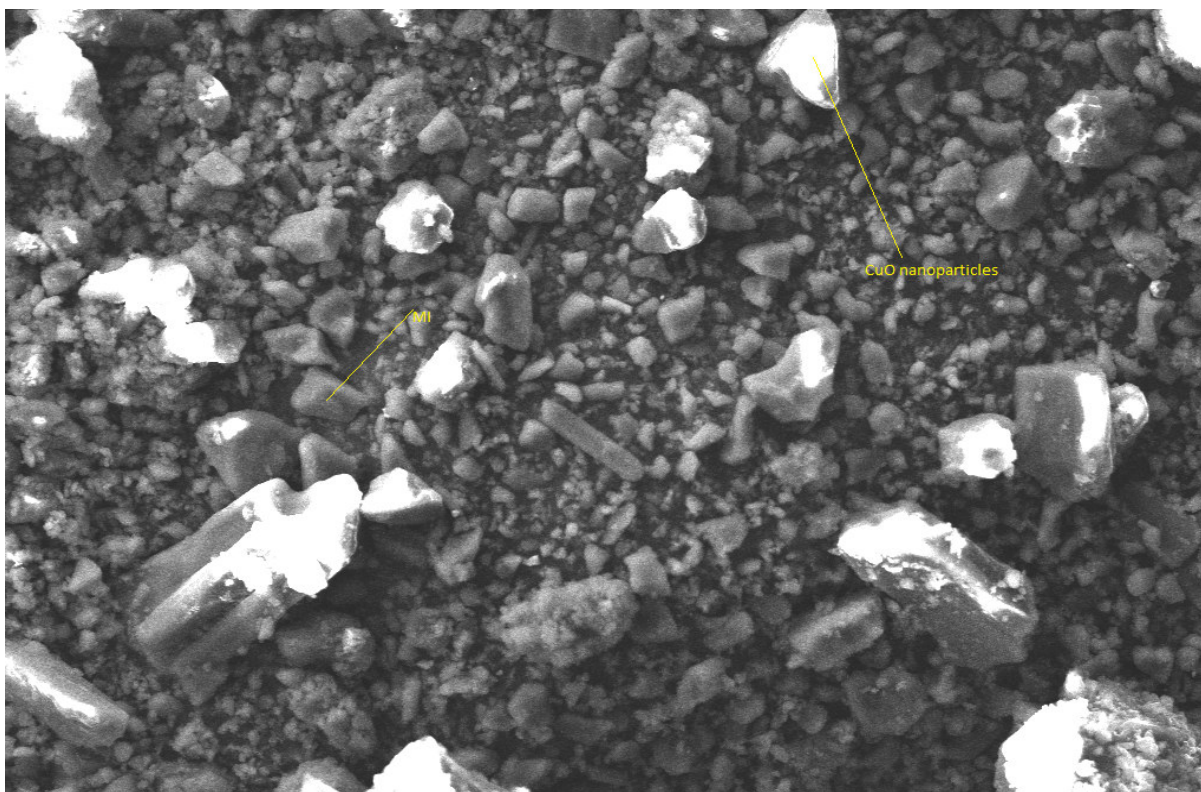
(a)

ACCEPTED MANUSCRIPT



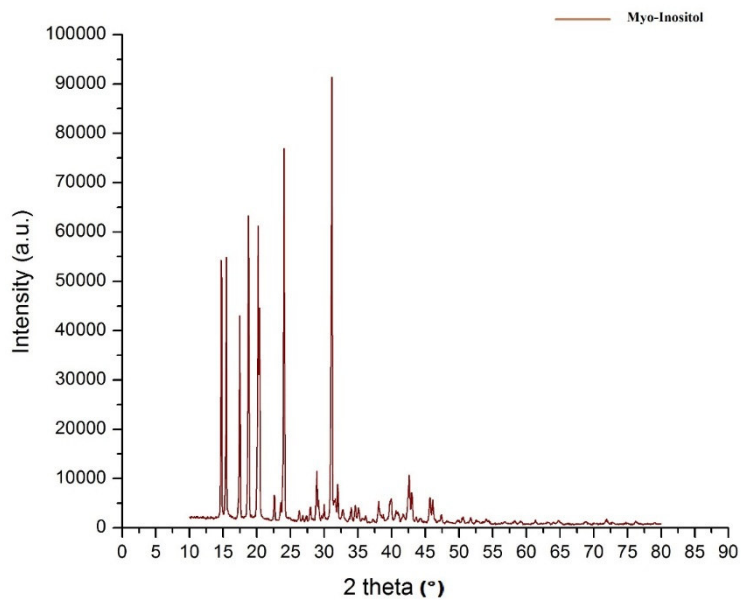
(b)

ACCEPTED

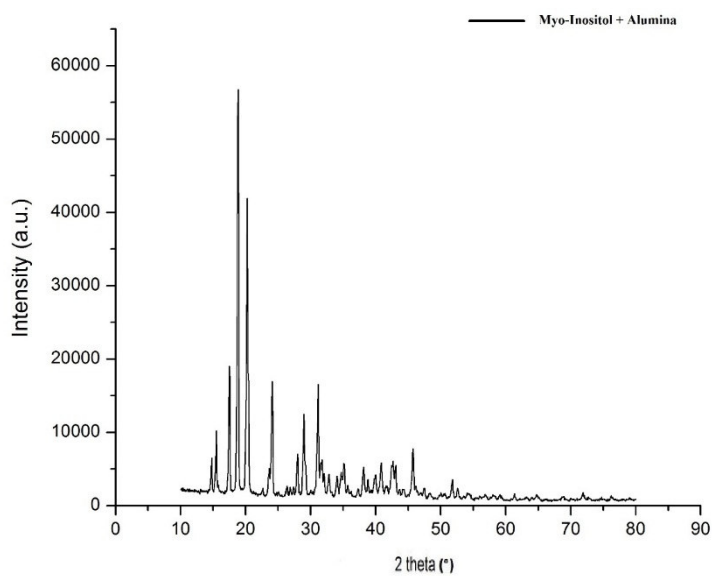


(c)

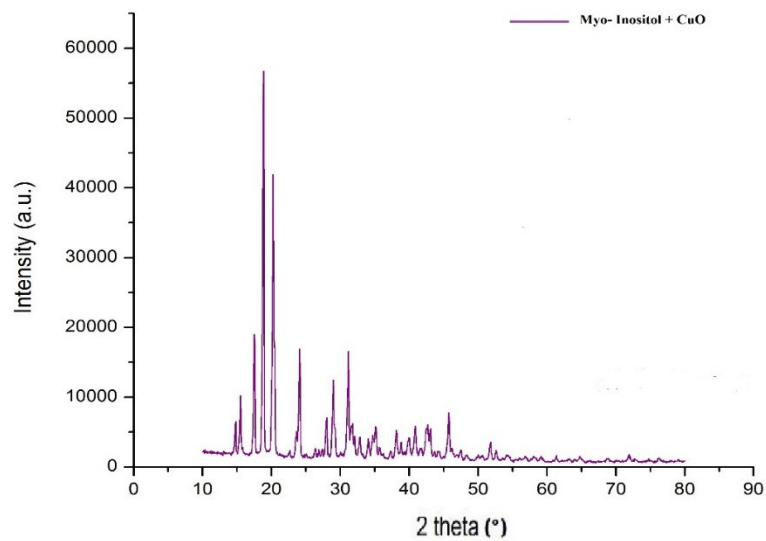
Fig. 3. SEM images at $\times 5,000$ magnification. SEM image of (a) Pure MI (b) MI-A and (c) MI-C



(a)

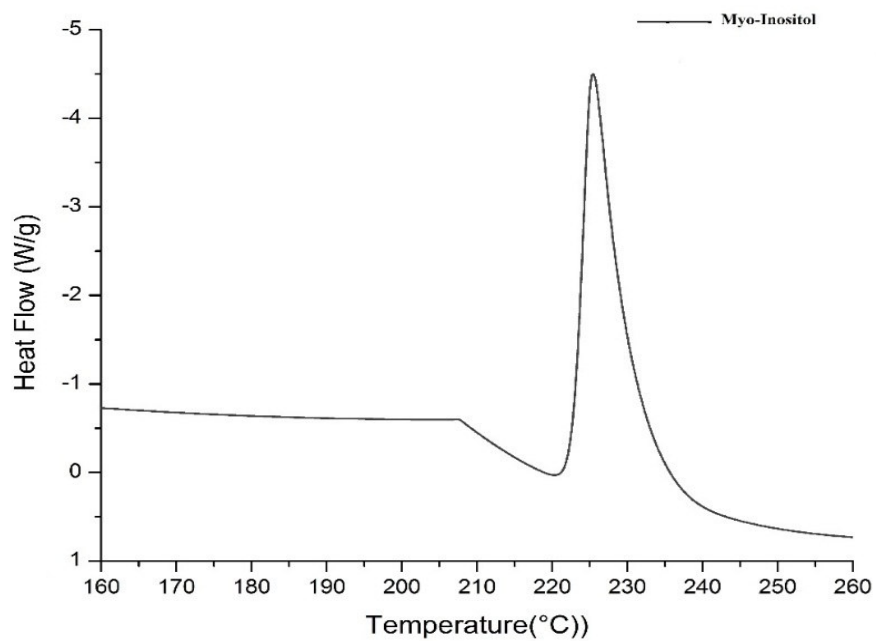


(b)

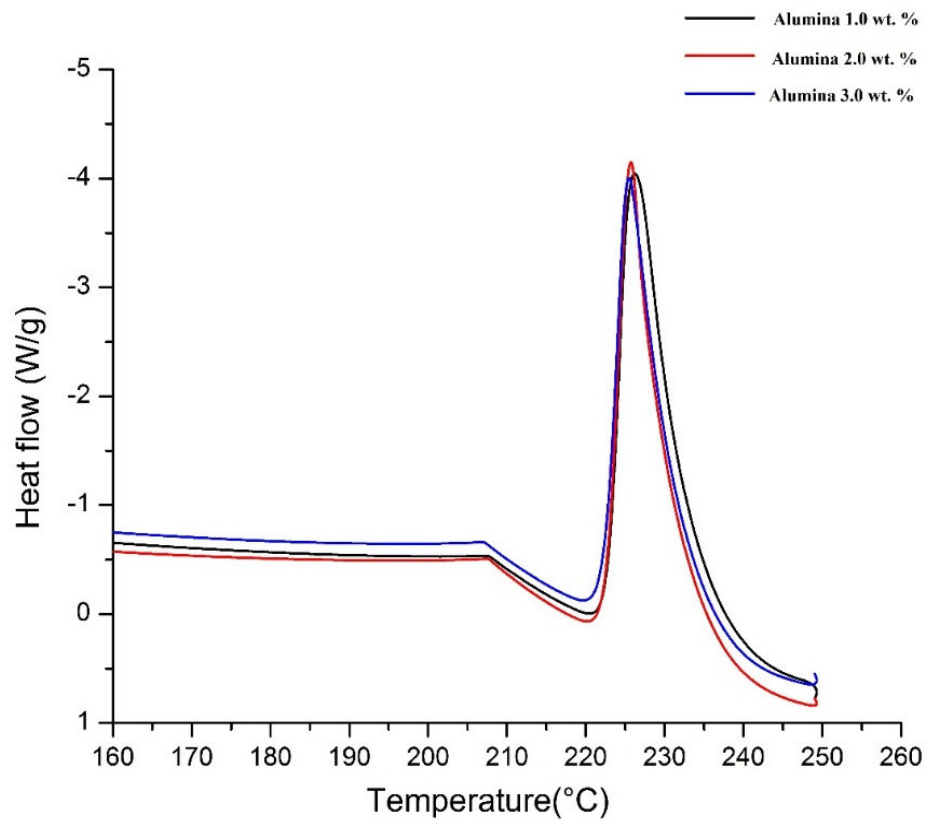


(c)

Fig. 4. XRD pattern (a) Pure MI (b) MI-A and (c) MI-C before thermal cycling

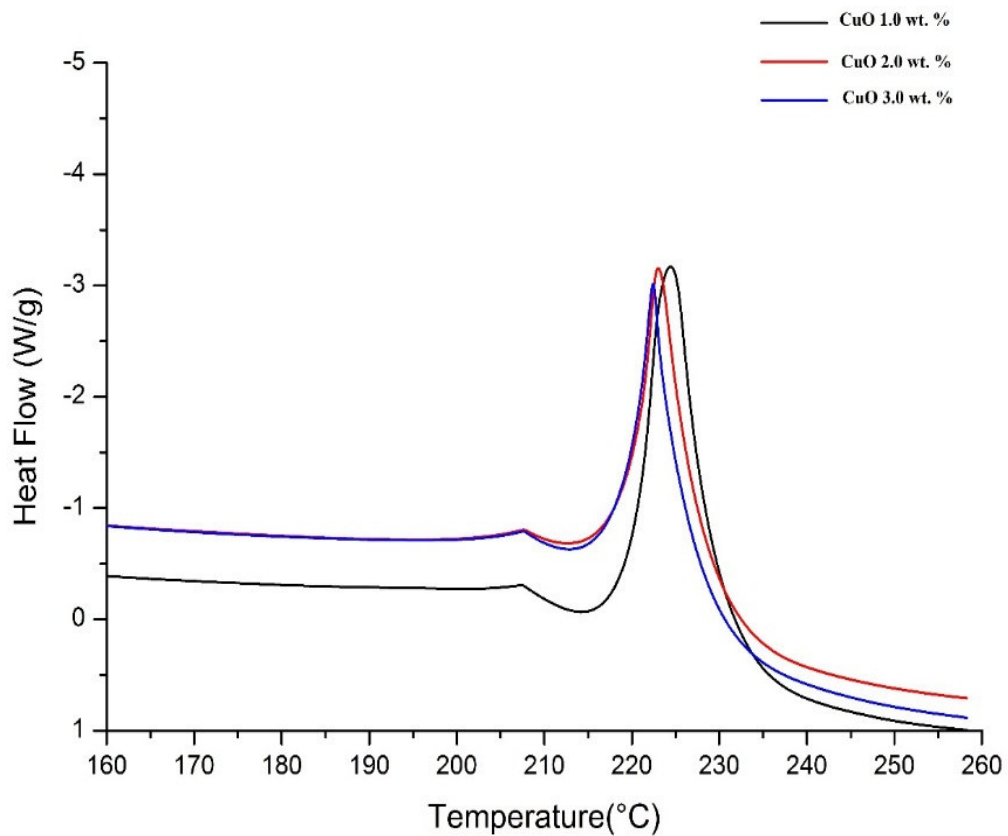


(a)



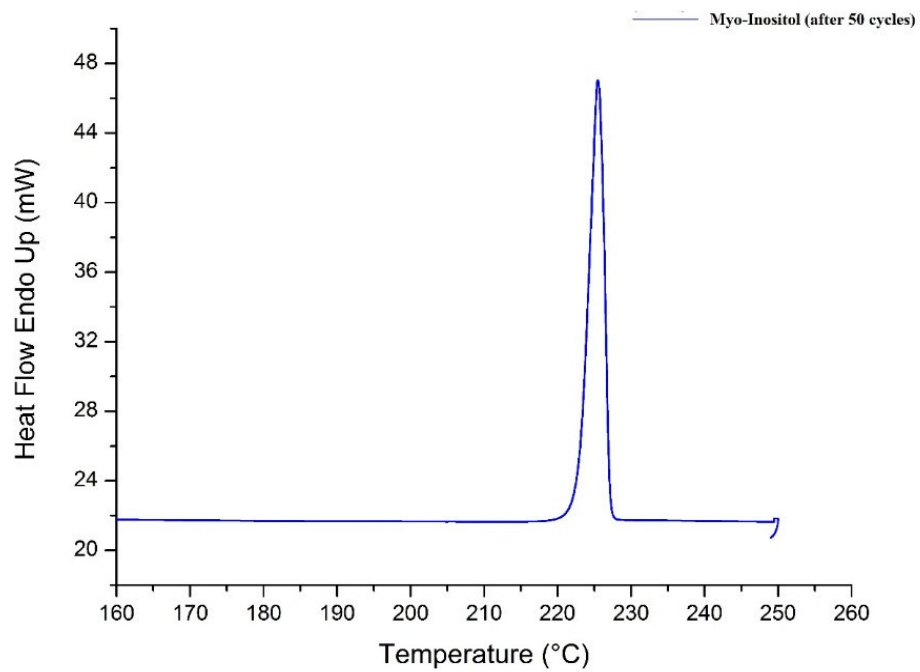
(b)

ACCEPTED



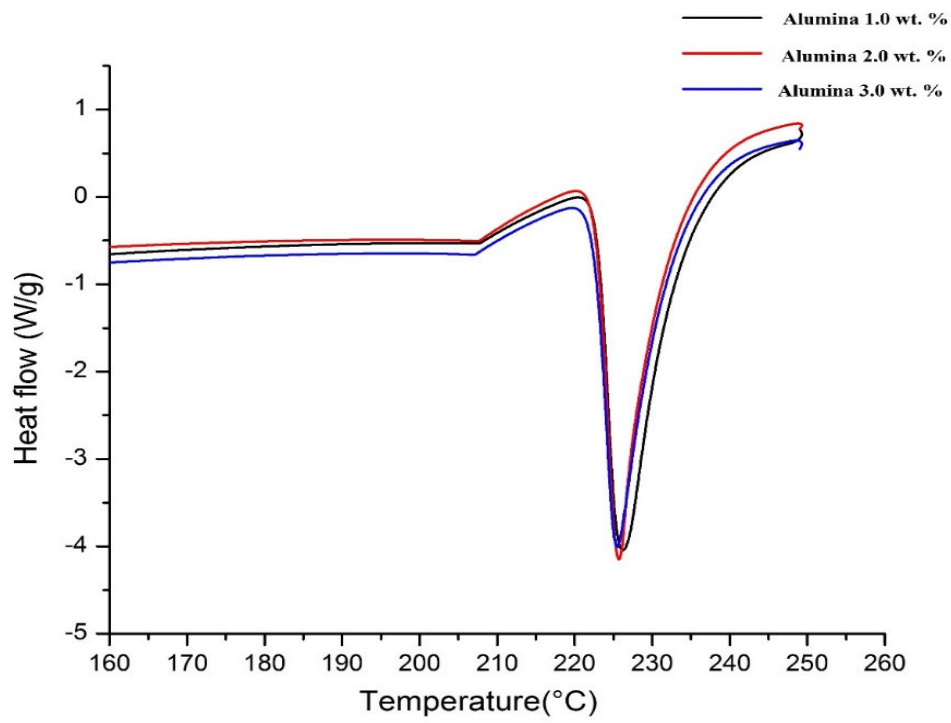
(c)

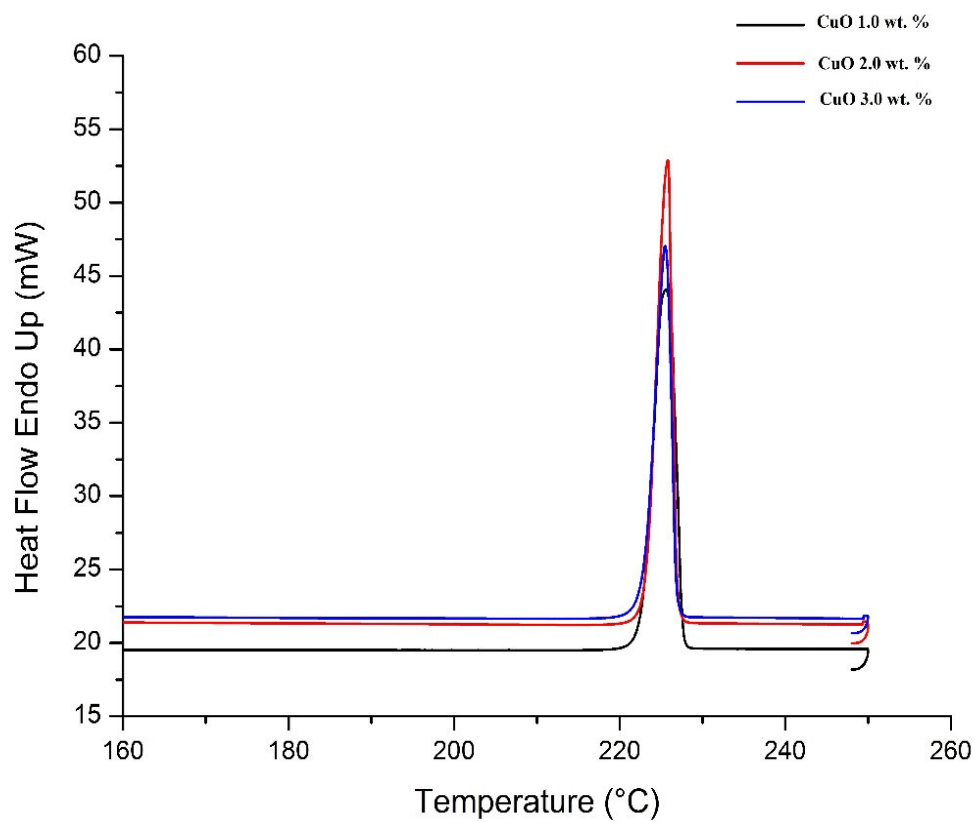
Fig. 5. DSC curves for (a) pure MI (b) MI-A (c) MI-C; all before thermal cycling



(a)

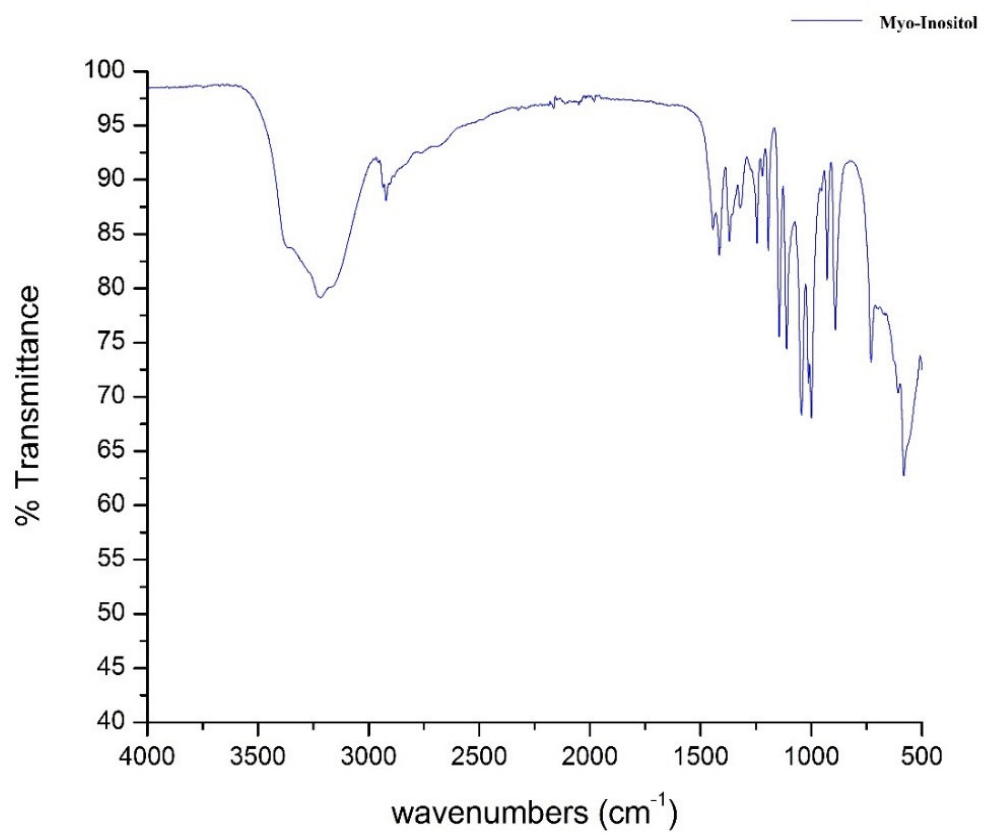
ACCEPTED MANUSCRIPT

ACCEPTED MANUSCRIPT
(b)



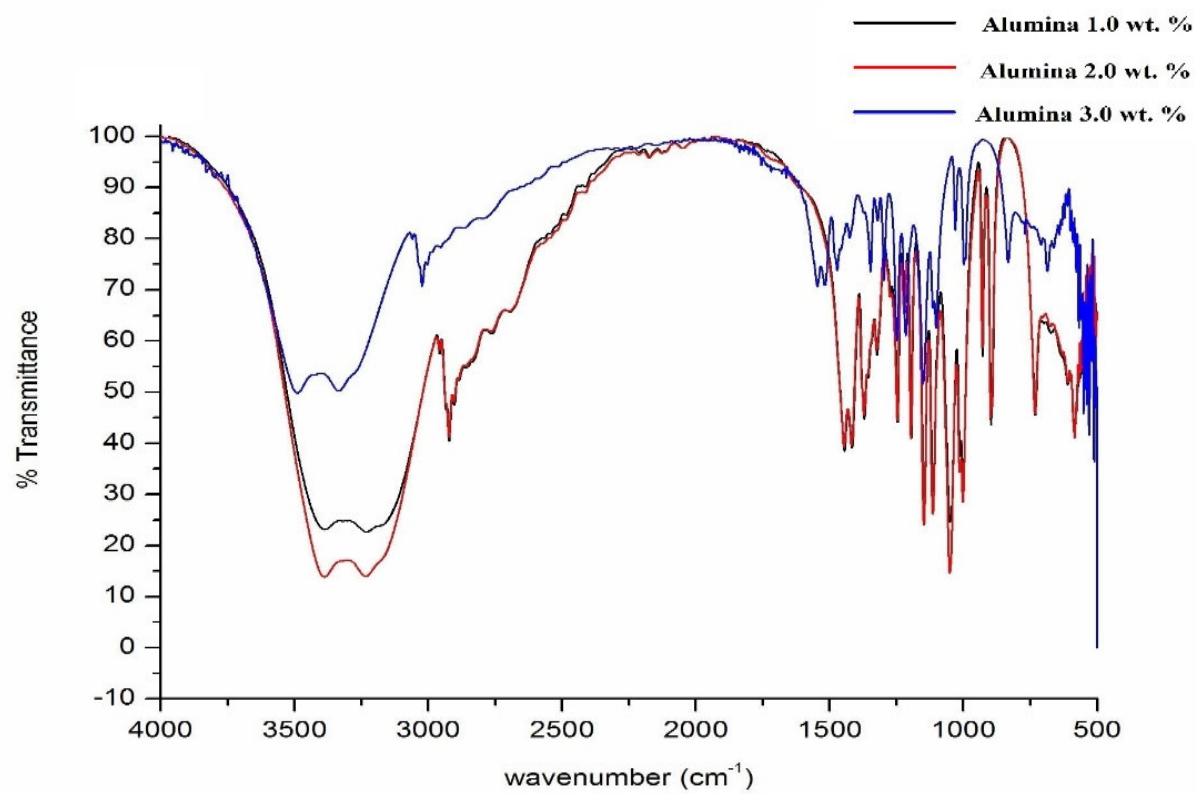
(c)

Figure 6. DSC curves for (a) Pure MI, (b) MI-A, and (c) MI-C; after 50 cycles



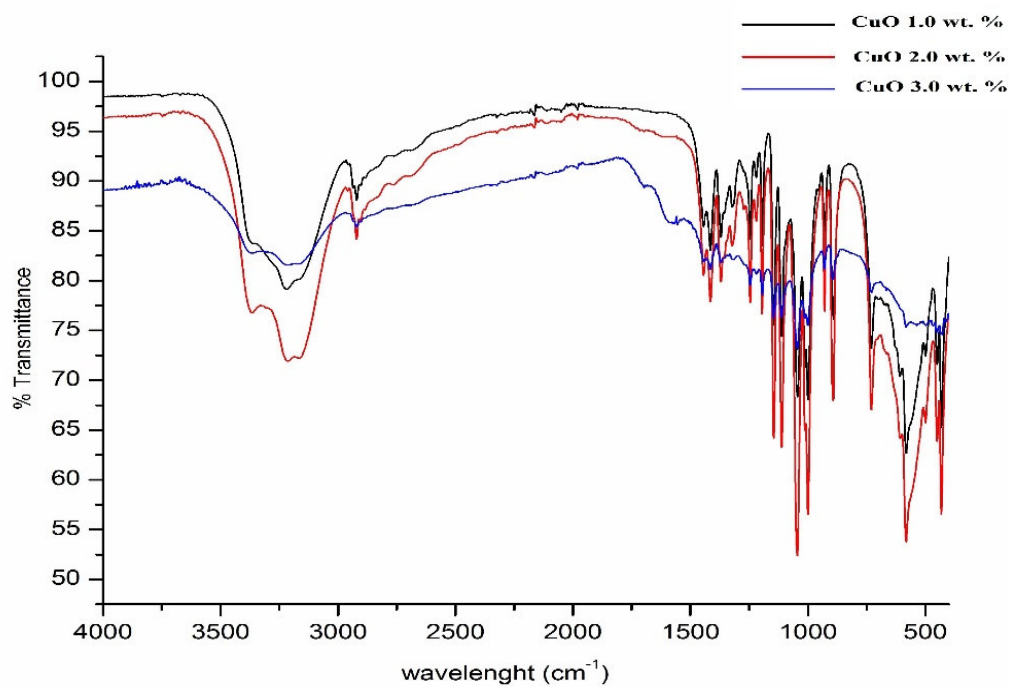
(a)

ACCEPTED



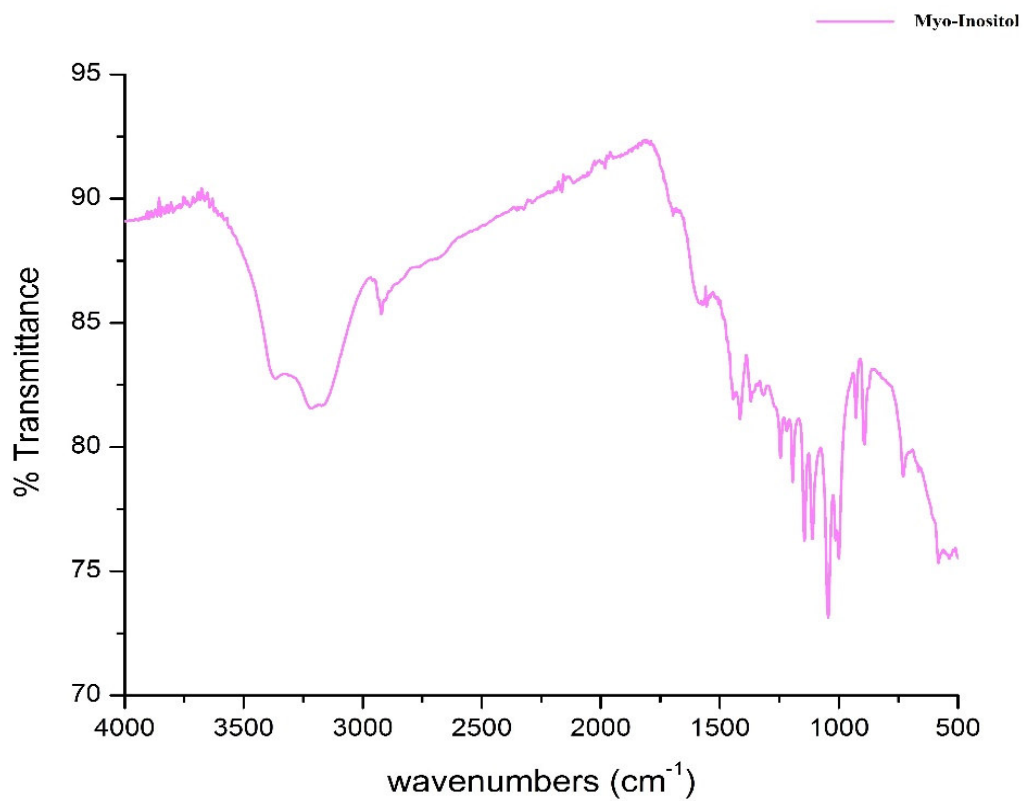
(b)

ACCEPTED MANUSCRIPT

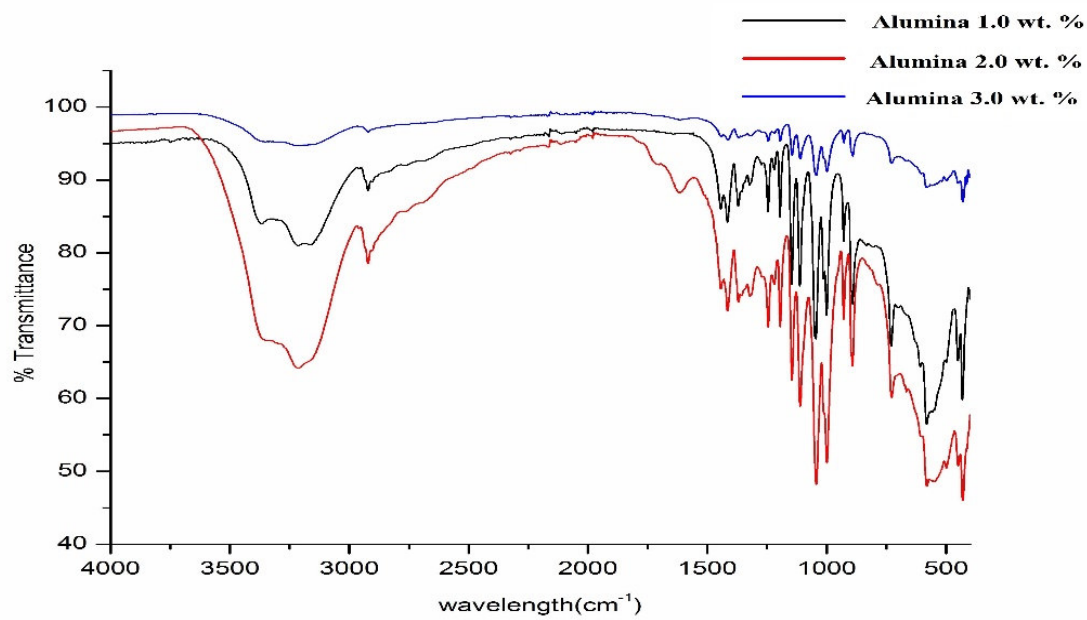


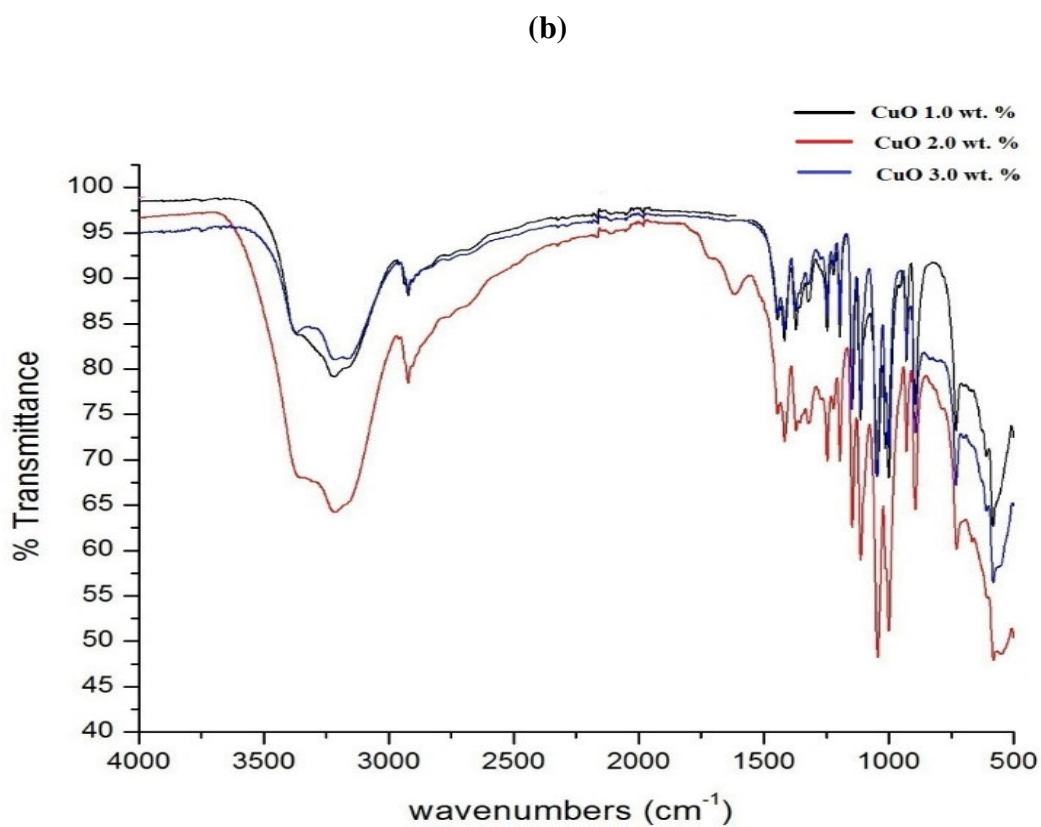
(c)

Fig. 7. FTIR measured transmission spectra before thermal cycling for (a) Pure MI, b) MI-A and (c) MI-C



(a)

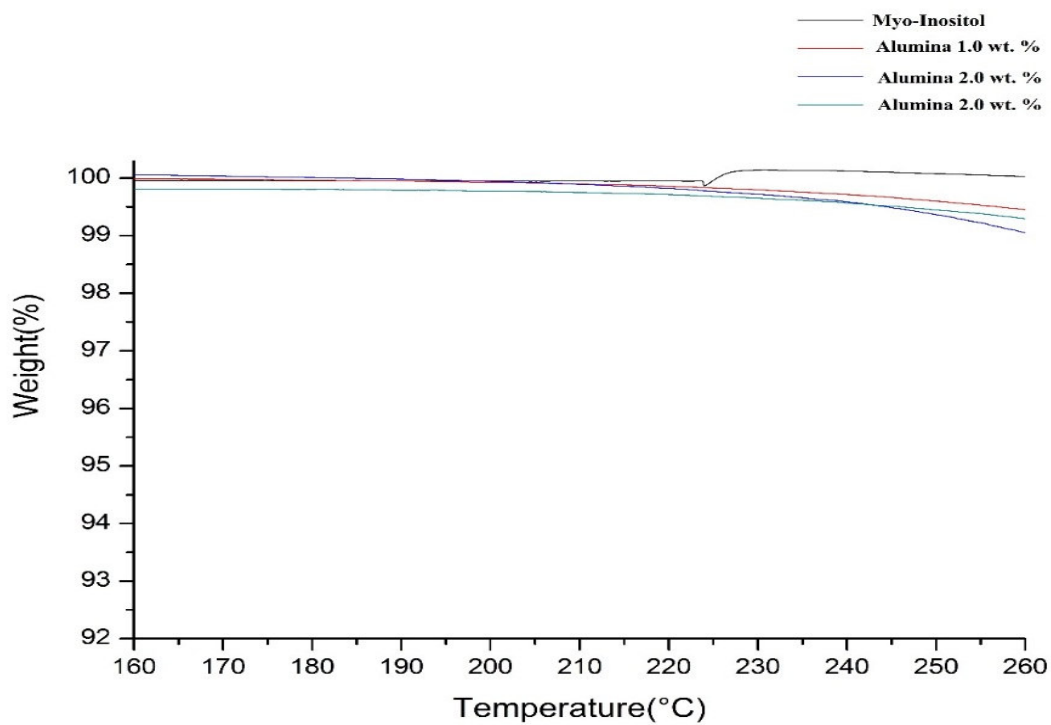




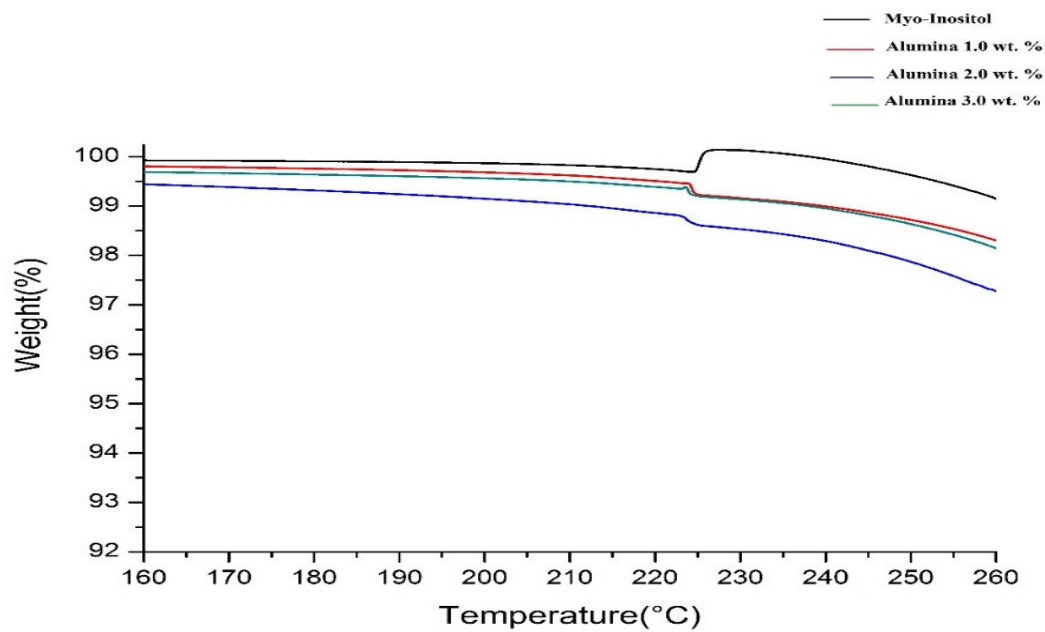
(c)

Figure 8. FTIR measured spectra after 50 thermal cycles for (a) Pure MI, (b) MI-A, and (c) MI-C

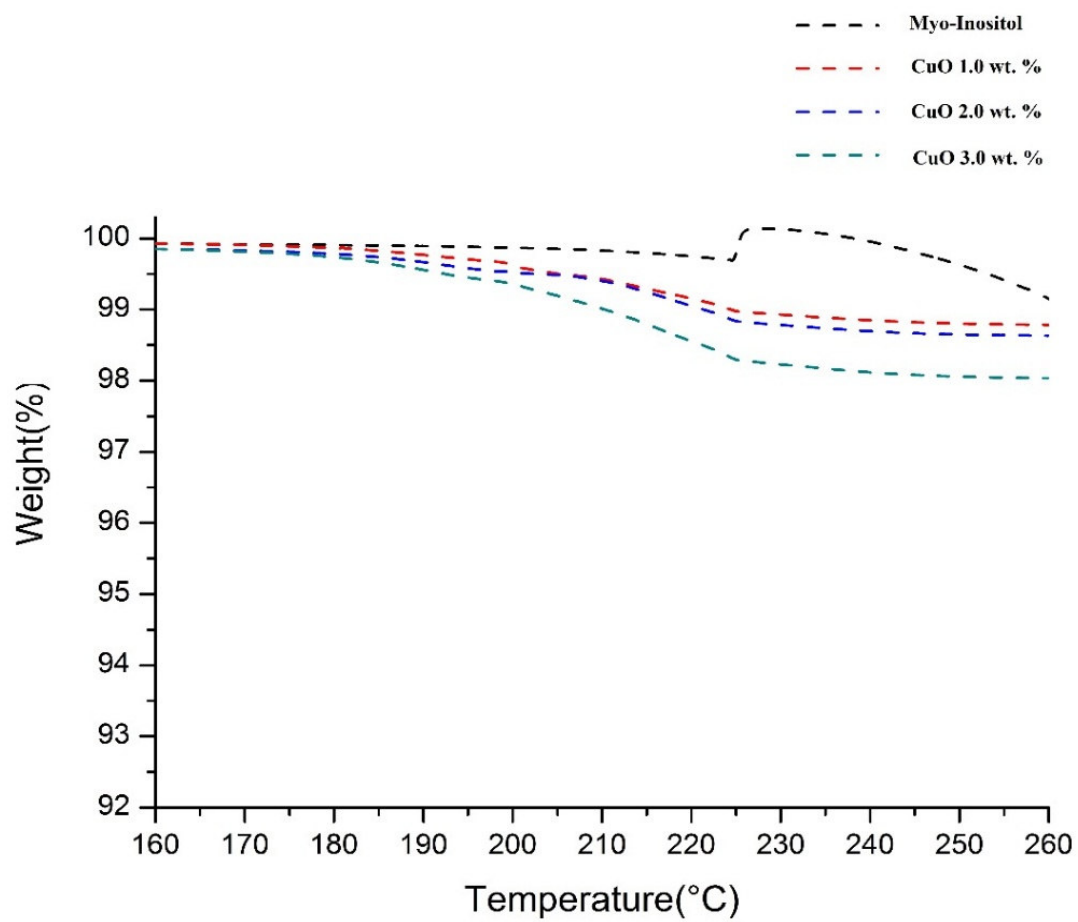
ACCEPTED MANUSCRIPT



(a)

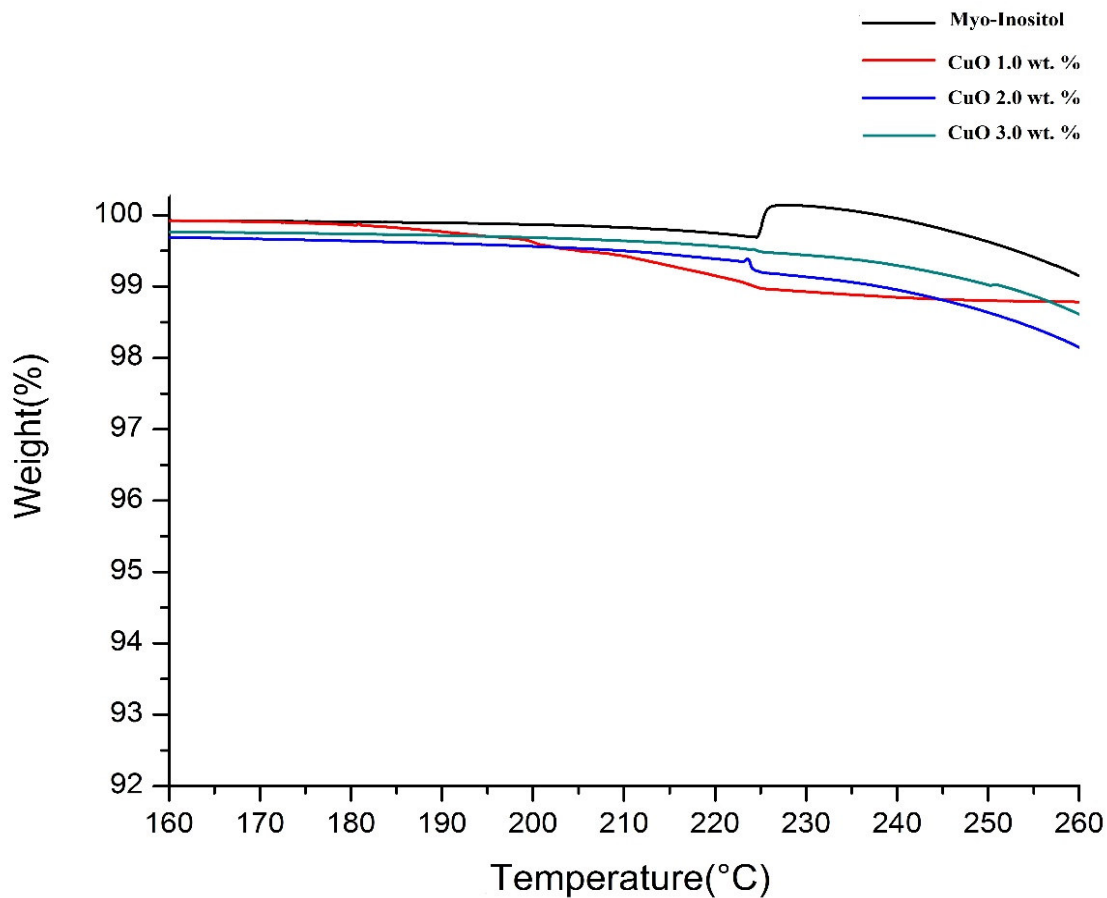


(b)



(c)

ACCEPTED



(d)

Figure 9. TGA curves for (a) Pure MI and MI-A before cycling, (b) Pure MI and MI-A after 50 cycles, (c) Pure MI and MI-C before cycling and (d) Pure MI and MI-C after 50 cycles